



Supersonically blown reduced graphene oxide loaded Fe–Fe₃C nanofibers for lithium ion battery anodes



Bhavana Joshi^{a,1}, Jong-Gun Lee^{a,1}, Edmund Samuel^a, Hong Seok Jo^a, Tae-Gun Kim^a, Mark T. Swihart^b, Woo Young Yoon^{c,**}, Sam S. Yoon^{a,*}

^a School of Mechanical Engineering, Korea University, Seoul, 02841, Republic of Korea

^b Department of Chemical & Biological Engineering, University at Buffalo, The State University of New York, Buffalo, NY 14260–4200, USA

^c Department of Materials Science & Engineering, Korea University, Seoul, 02841, Republic of Korea

ARTICLE INFO

Article history:

Received 17 February 2017

Received in revised form

19 July 2017

Accepted 28 July 2017

Available online 31 July 2017

Keywords:

Supersonic blowing

Fe–Fe₃C

Carbon nanofiber

Lithium ion battery

ABSTRACT

Reduced graphene oxide (rGO) loaded Fe–Fe₃C composite nanofibers were prepared via a supersonic blowing technique. After high temperature annealing, the resulting electrodes delivered an excellent reversible capacity of 558 mAh·g^{−1} at a current rate of 1500 mA g^{−1} at the 200th cycle. The supersonic blowing facilitated rapid and simultaneous coupling of exfoliated rGO with the solution-blown nanofibers, which is difficult to achieve by electrospinning methods. The performance of the fabricated electrode is remarkably high compared to the previously reported values; thus, these anodes are promising for application in lithium ion batteries.

© 2017 Elsevier B.V. All rights reserved.

1. Introduction

Transition metal oxides (TMOs) such as TiO₂, MnO, Fe₂O₃, Co₃O₄, NiO, and CuO, are widely used as anode materials in lithium ion batteries (LIB) [1]. These electrochemically-active TMOs exhibit high lithium storage capacity compared to traditional graphite [2]. However, TMOs suffer from fast capacity fading and poor rate capability at high current rates due to pulverization during the Li insertion/extraction process. To circumvent this issue, different nanoarchitectures [3] that afford a high surface area, a large number of reaction sites, and short paths for Li ion diffusion have been introduced [4]. Similar to TMOs, transition metal carbides (TMCs) have also been investigated as energy storage materials. TMCs have exhibited excellent catalytic activity leading to enhanced electrochemical performance [5], along with good electrical conductivity, mechanical properties, and reactivity [6]. TMCs are generally prepared by carbothermal reduction of the parent metals at high temperatures.

Among the TMCs, carbon-encapsulated iron nanoparticles, also known as *iron carbide* (Fe₃C) composites, have received substantial attention in the last few years due to their excellent electrochemical performance in Li storage [7]. Fe₃C has earned distinction in other applications based on its high hardness and good thermal stability [8]. The initial report of Fe₃C fabrication for LIB anode applications was presented by Su et al., where the core–shell composite exhibited a capacity of 500 mAh·g^{−1} at a current rate of 200 mA g^{−1} at the 30th cycle [9]. The authors reported that the Fe₃C-based electrode exhibited better electrochemical performance than traditional graphite. Although Fe₃C can only store 1/6 Li ions per unit, Fe₃C can act as a good catalyst for electrochemical reactions [9]. The catalytic role of Fe metal nanoparticles induces reversible transformation of the solid electrolyte interface (SEI) layer, ultimately resulting in enhanced capacity. Another Fe₃C nanocomposite derived from a metal organic framework was reported by Tan et al. [10]. In this case, MIL-100 was used as the Fe and carbon source. The composite delivered a capacity of 600 mAh·g^{−1} at a high current rate of 1000 mA g^{−1} after 100 cycles. The Fe–Fe₃C nanofibers reported by Li et al. [11] showed a capacity of 500 mAh·g^{−1} at the 50th cycle at a current rate of 200 mA g^{−1}. Chen et al. [12] reported the fabrication of Fe₃C anodes from a Fe precursor and resorcinol formaldehyde (RF) polymer via a hydrothermal method, achieving a capacity of 230 mAh·g^{−1} after 400 cycles

* Corresponding author.

** Corresponding author.

E-mail addresses: wyyoon@korea.ac.kr (W.Y. Yoon), skyyoon@korea.ac.kr (S.S. Yoon).

¹ These authors have contributed equally.

at a current rate of 2000 mA g^{-1} . An in-situ generated non-graphitic C/Fe₃C composite reported by Zhao et al. [8] provided a capacity of 350 mAh g^{-1} at a current rate of 1000 mA g^{-1} during the rate capability test. These aforementioned studies used a variety of nanostructures that are not amenable to commercial production, because their fabrication processes are complex and they require binders that hamper the performance and capacity of the LIB cells [13].

Herein, a supersonic blowing technique is used to fabricate reduced graphene oxide (rGO) loaded Fe-Fe₃C composite nanofibers. This technique facilitates rapid and simultaneous coupling of the solid secondary particles (i.e., rGO) with solution-blown nanofibers. Such structures are not easily achieved by electro-spinning, as the higher loading of rGO blocks the spinning tip. The supersonic blowing approach has not previously been used for LIB anode production. We report here the fabrication of rGO/Fe-Fe₃C nanofibers by supersonically blowing graphene with a polymeric solution of Fe. Supersonic blowing causes exfoliation of the graphene flakes and locking with the Fe-containing nanofibers. Further carbonization of the fibers in an argon gas environment generates a mixture of metallic Fe and Fe₃C phases, as determined by X-ray diffraction (XRD). The fibers are produced and deposited rapidly, and improved efficiency of the LIB electrode is achieved with lower processing costs.

2. Experimental

The supersonic kinetic spraying setup used for fabrication of rGO/Fe-Fe₃C NF is illustrated in Fig. 1. In this system, compressed air is injected into a nozzle at a pressure of 4 bar via a hot tube that heats the air to 200°C . This gas is accelerated in the converging section of the nozzle and attains supersonic speed in the diverging section of the nozzle and at the nozzle exit. The nozzle dimensions and other details of the apparatus are those reported in our earlier paper [14]. A solution of 8 wt% of polyacrylonitrile (PAN, $M_w = 150 \text{ kDa}$, Sigma-Aldrich) and 9.2 g of *N,N*-dimethylformamide (DMF, 99.8%, Sigma-Aldrich) was prepared and homogenized for 24 h at 60°C . It was later mixed with 4 wt % iron (III) acetylacetonate ((FeAcAc), Fe(C₅H₇O₂)₃, Sigma-Aldrich). In a separate container, 0.25 g of rGO flakes was mixed with 40 ml of DMF. The samples without rGO and with rGO are termed Fe-1 (Fe-Fe₃C nanofiber) and Fe-2 (Fe-Fe₃C/rGO nanofiber), respectively.

The precursor solution of Fe was supplied by means of a syringe pump (KDS LEGATO 100) and the rGO solution was simultaneously supplied to the supersonic stream by another syringe pump; the respective flow rates were 0.8 and 2.4 ml min^{-1} . In the supersonic stream, the Fe solution is stretched due to the viscosity of the polymer PAN, thereby producing fibers and generating an increase in surface area of the sample; the fibers are then swept onto a Cu foil placed at a distance of 70 mm from the nozzle exit. Simultaneously, the rGO sheets are also sprayed and become intertwined in a 3D array with the Fe nanofibers, as shown later. The upstream chamber pressure and temperature of the supersonic stream were $P_0 = 4 \text{ bar}$ and $T_0 = 250^\circ\text{C}$, respectively. Although supersonic spraying was performed with a high temperature gas jet, much of the thermal energy is converted into kinetic energy within the nozzle. Thus, the static temperature near the substrate is only slightly above room temperature, which is why this process is also called “cold spray” deposition. With this low substrate temperature, the supersonically blown nanofibers are deposited on the copper substrate by high-velocity impactation, with high kinetic energy. Compaction of the film upon impact produces strong adhesion, mainly through van der Waals interactions of molecules and materials in intimate contact.

After completion of the nanofiber coating process, the samples were carbonized for 2 h at 700°C in a tube furnace under flowing argon. The required annealing temperature was achieved by ramping the temperature from room temperature at a rate of 3°C min^{-1} . The carbonization process transforms the PAN nanofiber to a conductive carbon matrix that is beneficial for charge transport in LIB. The resulting carbonized black colored samples were punched into discs with a diameter of 14 mm, as shown in Fig. 1.

2.1. Electrochemical tests

The electrochemical performance was measured in a CR2032 coin-type half-cell, where the 14-mm-diameter carbonized binder-free NF mats were directly applied as anodes without a slurry-coating process. A metallic Li sheet was used as the reference electrode. A microporous polyethylene film (Celgard 2400; Celgard, South Korea) was used as the separator between the two electrodes. The electrolyte was 1-M LiPF₆ in a solvent mixture of ethylene carbonate (EC), dimethylcarbonate (DMC), and ethyl

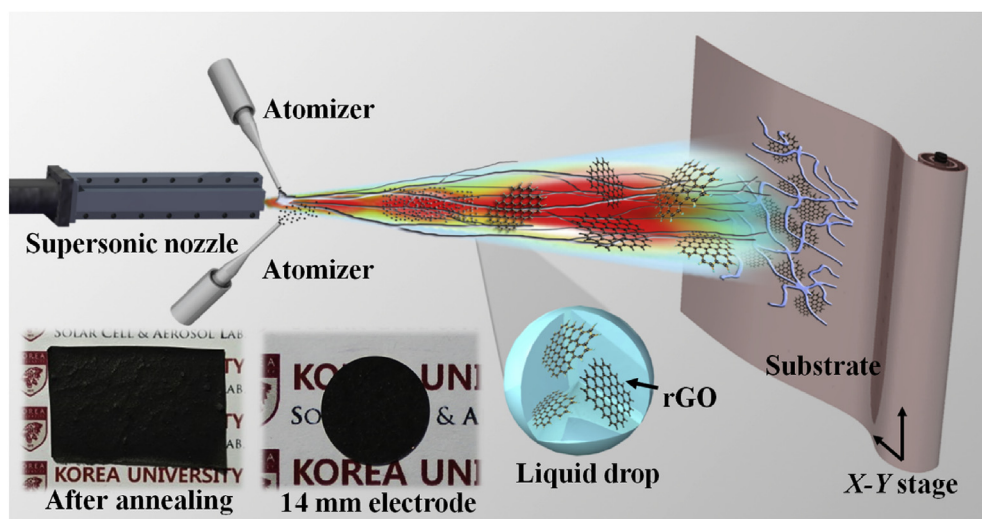


Fig. 1. Supersonic kinetic spraying process used for LIB electrode preparation.

methyl carbonate (EMC) (1:1:1 by volume) (PuriEL Soulbrain, Seongnam, South Korea). Galvanostatic discharge/charge curves were measured at 25 °C using a WBCS3000 battery cycler system (WonATech, South Korea). The specific capacity was calculated with respect to the mass of Fe_3C and rGO. The cells were initially subjected to rate testing at different current densities (5 cycles each at 500 mA g^{-1} , 1000 mA g^{-1} , 2000 mA g^{-1} , and 5000 mA g^{-1}) followed by an additional cycle test at 500 mA g^{-1} . In total, the number of cycles tested was 80. The long-term cycling tests were also conducted at current rates of 1500 and 200 mA g^{-1} . Electrochemical impedance spectroscopy (EIS) measurements were performed using a potentiostat (VersaSTAT-3, Princeton Applied Research, USA) with a small sinusoidal perturbation of 10 mV over a frequency range of 100 kHz to 10 mHz .

2.2. Characterization

The prepared and carbonized fibers were characterized to determine their structural, morphological, chemical, and electrochemical properties. X-ray diffraction (XRD, SmartLab, Rigaku) was used to study the crystalline structures of the mats. X-ray photoelectron spectroscopy (XPS, Theta Probe Base System, Thermo Fisher Scientific Co.) measurements were conducted to evaluate the chemical states of elements in the mats. The surface morphologies and elemental mapping of the fabricated mats were evaluated using a field emission scanning electron microscope (FE-SEM, S-5000, Hitachi, Ltd.) and a transmission electron microscope (TEM, JEM 2100F, JEOL Inc.). The surface roughness of film was measured by an optical profiler (Veeco, NT-1100, USA). A confocal Raman spectrometer (NRS-3100, Jasco) was used to analyze the carbon content and amount of carbon defects in the mats.

3. Results and discussion

The X-ray diffraction (XRD) patterns of the annealed Fe 1 and Fe 2 samples are presented in Fig. 2(a), showing peaks at $2\theta = 37^\circ$, 43° and 44.9° (JCPDS-35-0772). These peaks confirm the formation of Fe_3C , whereas the peak at $2\theta = 44.7^\circ$ (JCPDS-87-0722) corresponds to metallic Fe. This confirms the formation of the Fe- Fe_3C mixture of phases when the fibers are carbonized under argon gas at 700°C . Additionally, in Fe-1, a peak at 50.5° corresponds to Fe_5C_2 (JCPDS-20-0508). These results are consistent with previous reports [8,15]. The broad hump centered near $2\theta = 25^\circ$ is derived from carbon from PAN and rGO. Further, the presence of graphene and carbonization of PAN were detected using Raman spectral analysis of Fe-2 (Fig. 2(b)), which revealed distinguishable peaks at 1349 and 1586 cm^{-1} , respectively, corresponding to the D (disordered carbon) and G (crystalline graphene) bands. The D-to-G band intensity ratio (I_D/I_G) was 1.06 , which indicates that the disorder in this case, is mainly due to carbonization of PAN and Fe_3C formation. The broad peak observed at 2868 cm^{-1} is related to the 2D band of graphene.

Scanning electron microscope (SEM) images of Fe 1 and Fe 2 are presented in Fig. 2 (c) and (d) respectively. The insets present magnified views of the samples. These fibers are random in shape, but are interconnected well throughout the network, providing increased electrochemical sites that enhance interfacial interactions between Li-ions and an electrolyte. The SEM of Fe-2 shows the entanglement of graphene in a thin, wrinkled structure to generate a 3D morphology. The average fiber diameters are $480 \pm 50 \text{ nm}$ and $460 \pm 50 \text{ nm}$ for Fe-1 and Fe-2, respectively, based on the measurement of 200 fibers taken from SEM images. Fig. 2(d) shows that empty areas between fibers can be filled by graphene sheets. The cross-sectional SEM image of Fe-2 presented in Fig. S1

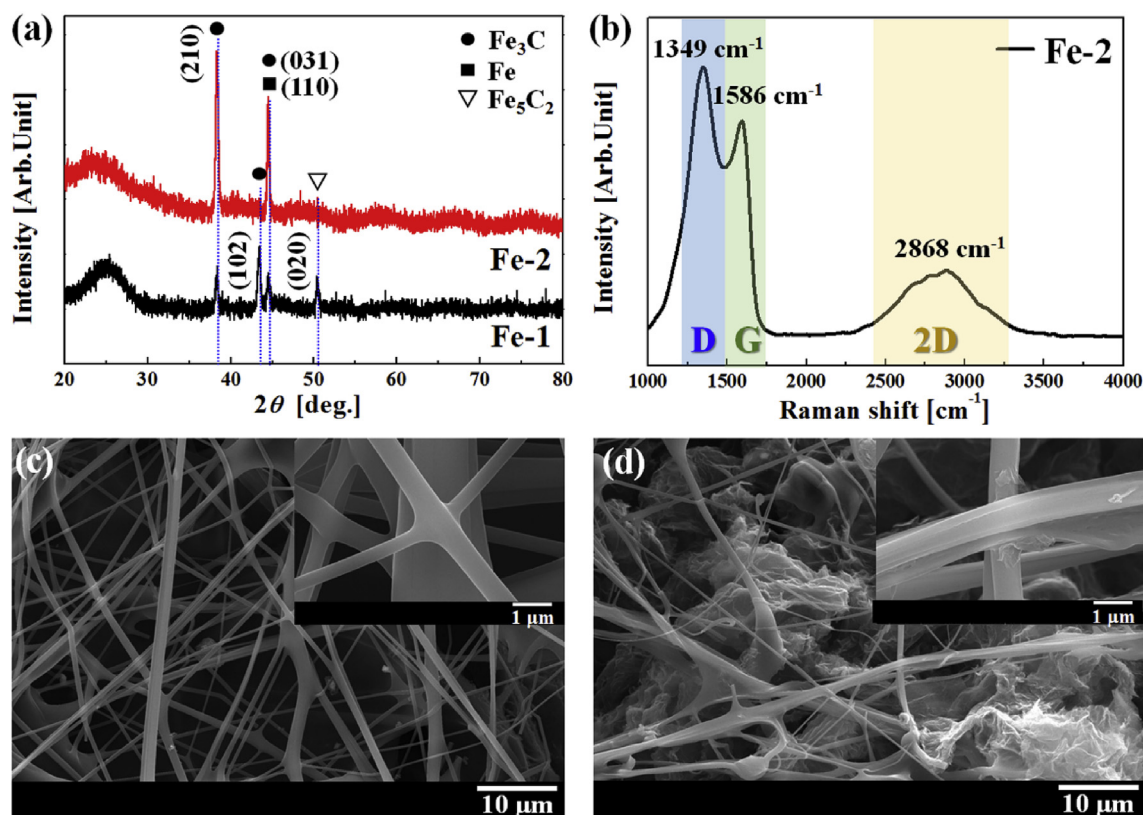


Fig. 2. (a) XRD patterns of Fe-1 and Fe-2, (b) Raman spectra, and surface morphology of (c) Fe-1, (d) Fe-2.

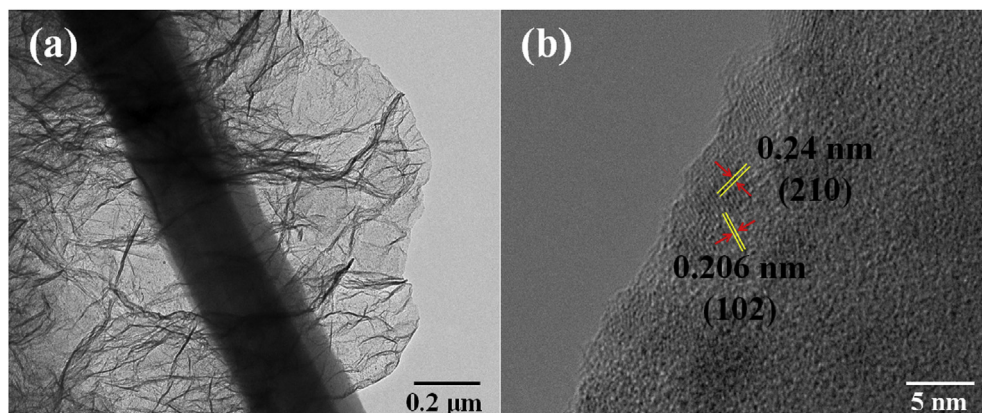


Fig. 3. (a) TEM and (b) HRTEM image of Fe-2.

confirms the entanglement of graphene with Fe nanofibers. The surface roughnesses of Fe-1 and Fe-2 were measured using an optical profiler. As shown in Fig. S2, this revealed an increase in surface roughness after inclusion of graphene.

Fig. 3(a) displays a TEM image of the solution blown nanofibers entangled with a rGO sheet. The high-resolution transmission electron microscope (HRTEM) image in Fig. 3(b) indicates lattice spacings of 0.24 nm and 0.206 nm, which correspond to the (210) and (102) planes of Fe_3C [15].

The elemental mapping images presented in Fig. 4(a)–(c) confirm the presence of Fe and C along with a small proportion of O, confirming that the nanofibers were composed mainly of the Fe_3C phase. Importantly, the distribution of Fe and C along the fiber was uniform. Fig. 4(e) shows the deconvoluted high-resolution XPS

spectrum of Fe 2p with a peak at 707.5 eV that is related to metallic iron (Fe^0). The Fe $2p_{3/2}$ peaks at 709.8 and 712.5 eV are associated with Fe in the form of Fe^{2+} and Fe^{3+} , respectively. The broad peak between 720 and 726 eV is attributed to Fe $2p_{1/2}$ which is further deconvoluted into contributions from Fe^{2+} and Fe^{3+} . Other Fe^{3+} and Fe^{2+} shakeup satellite peaks were also observed [16]. The deconvoluted C 1s spectrum (Fig. 4(d)) shows a peak at 284.5 eV, indicative of sp^2 hybridized graphitic carbon ($\text{C}=\text{C}$) and the other peak at 286.2 eV that originates from carbon bonded to oxygen atoms [17]. Furthermore, the O 1s spectrum presented in Fig. 4(f) shows three deconvoluted peaks at 531, 532.2, and 535 eV, corresponding to iron oxide and oxygen linked with carbon; slight oxidation of Fe and carbon on the surface may result from exposure to atmospheric oxygen and moisture. From XPS, the atomic

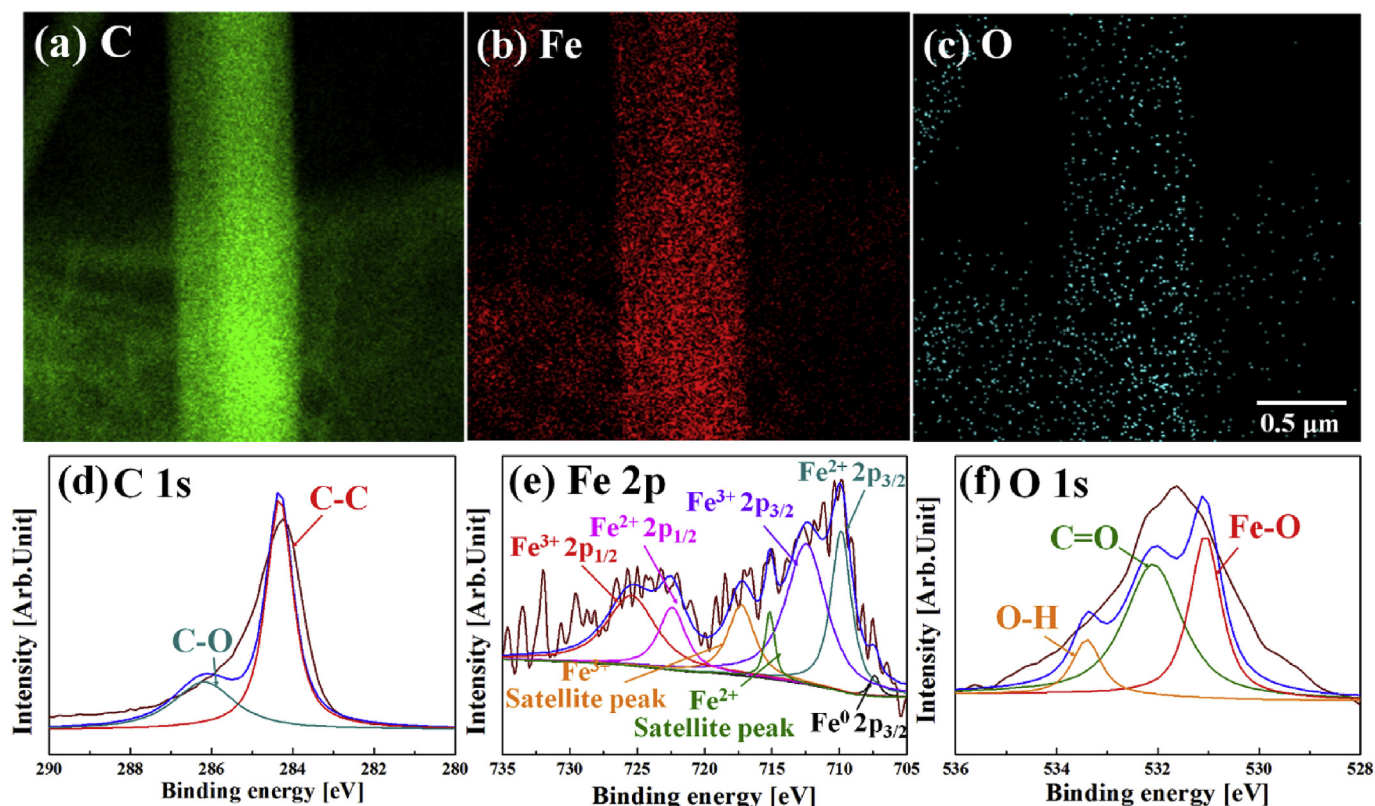


Fig. 4. Elemental composition of the Fe-2 sample for (a) carbon, (b) Fe, and (c) O. High-resolution XPS spectrum of (d) C 1s, (e) Fe 2p, and (f) O 1s of the Fe-2 sample.

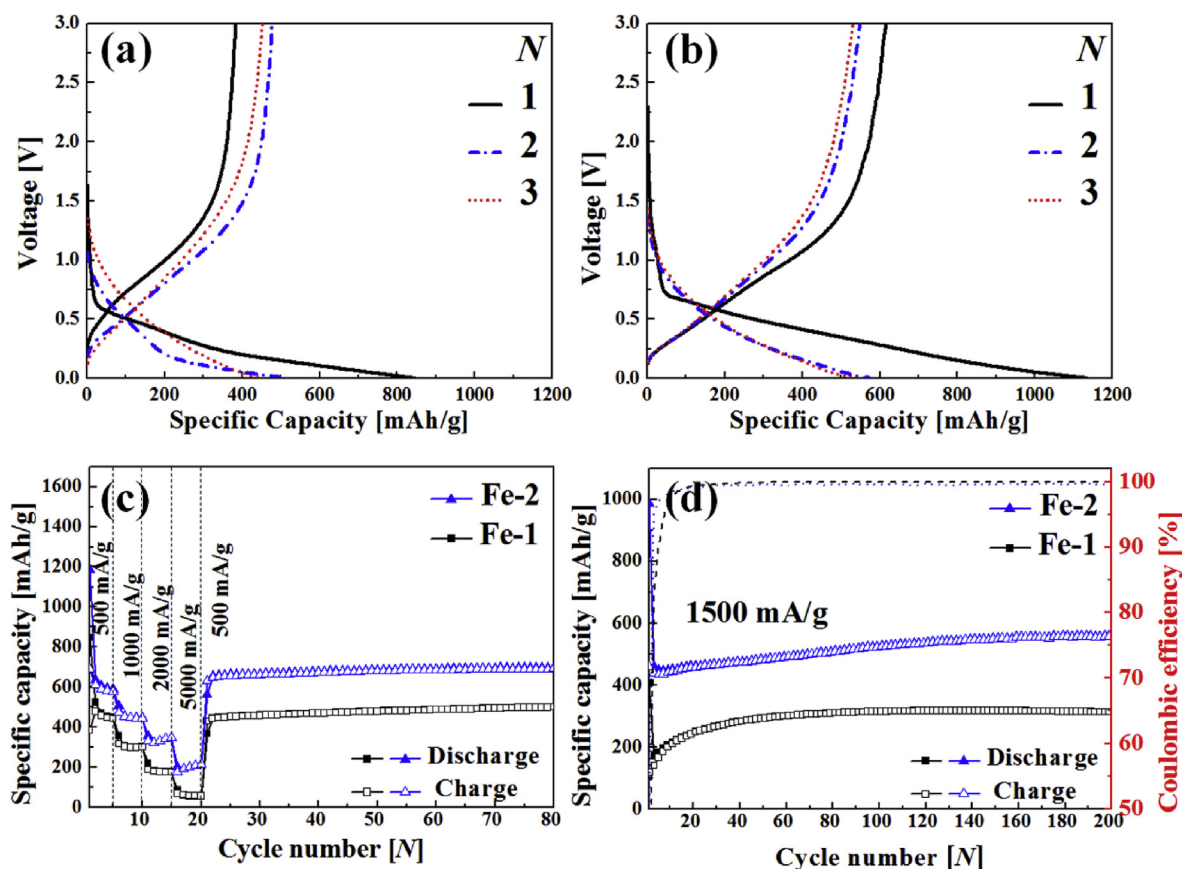


Fig. 5. Discharge-charge curves of (a) Fe-1 and (b) Fe-2 at 500 mA g⁻¹ for N = 1, 2, and 3. (c) Rate capability over a voltage range of 0.01–3.0 V. (d) Long-term cycle performance and Coulombic efficiency at 1500 mA g⁻¹.

concentration of each element was 88.7, 4.2, and 7.1% for C 1s, O 1s, and Fe 2p, respectively.

The electrochemical performance of the CR2032 coin cells employing Fe-1 and Fe-2 as electrodes were separately investigated as shown in the discharge/charge curves for the 1st, 2nd, and 3rd cycles in Fig. 5. Fig. 5(a) demonstrates that the Fe-1 sample delivered first discharge/charge capacities of 850 and 395 mAh·g⁻¹, respectively, with a Coulombic efficiency of ~46%. In comparison, the Fe-2 electrode fabricated by with rGO incorporated in nanofibers delivered very high first discharge/charge capacities of 1180 and 690 mAh·g⁻¹, respectively with a Coulombic efficiency of ~58% as shown in Fig. 5(b). In both cases, the current density was maintained at 500 mA g⁻¹. The lower initial Coulombic efficiency is due to irreversible electrolyte reduction and formation of a SEI layer, contributing to high capacity during the first discharge cycle.

The Coulombic efficiency of Fe-2 is improved as compared to Fe-1 because of the enhanced electrical conductivity provided by including rGO, which reduces the charge transfer resistance. This reduced charge transfer resistance will be later confirmed and discussed using a Nyquist plot. A steep drop of voltage was observed between 1.0 and 0.6 V in the first discharge curve in both cases. However, the discharge curves in the second cycle were different from the first discharge curves, which may reflect formation of a stable SEI film. The long and stable plateau at 0.8 V, which is normally observed in Fe₂O₃ does not appear in these results, consistent with the presence of Fe₃C, and absence of iron oxides. The Coulombic efficiency increased to ~95% in the second cycle [18]. The benefit of the solution blown technique is clearly revealed by comparing results from Fig. S3(a) (electrospun CNF) and Fig. 5(a) (solution blown CNF); the specific capacity of the

Table 1
Comparison of the specific capacity of the present film with literature values.

Composition	Method & Electrode prepared	First discharge capacity [mAh·g ⁻¹]	First reversible capacity [mAh·g ⁻¹]	Reversible capacity (N th) [mAh·g ⁻¹]	Current rate [mA·g ⁻¹]	Refs.
Fe-Fe ₃ C	ES, Nanofiber w/Binder	980	890	500 (70)	200	[11]
C/Fe-Fe ₃ C	GR, nanocomposite w/binder	850	425	382 (30)	200	[9]
Graphene/Fe-Fe ₃ C	HT, Nanocomposite w/Binder	904	222	1098 (50)	100	[10]
Fe ₃ C	HT, Composite w/Binder	250	225	316 (250)	1000	[12]
C/Fe-Fe ₃ C	PP, Composite w/Binder	1246	763	750 (120)	100	[8]
rGO/Fe-Fe ₃ C	Nanofiber w/o binder	985	485	558 (200)	1500	Present
rGO/Fe-Fe ₃ C	Nanofiber w/o binder	1697	994	992 (60)	200	Present

ES – Electrospinning, GR – green route synthesis, HT – hydrothermal, PP – Polymerization pyrolysis.

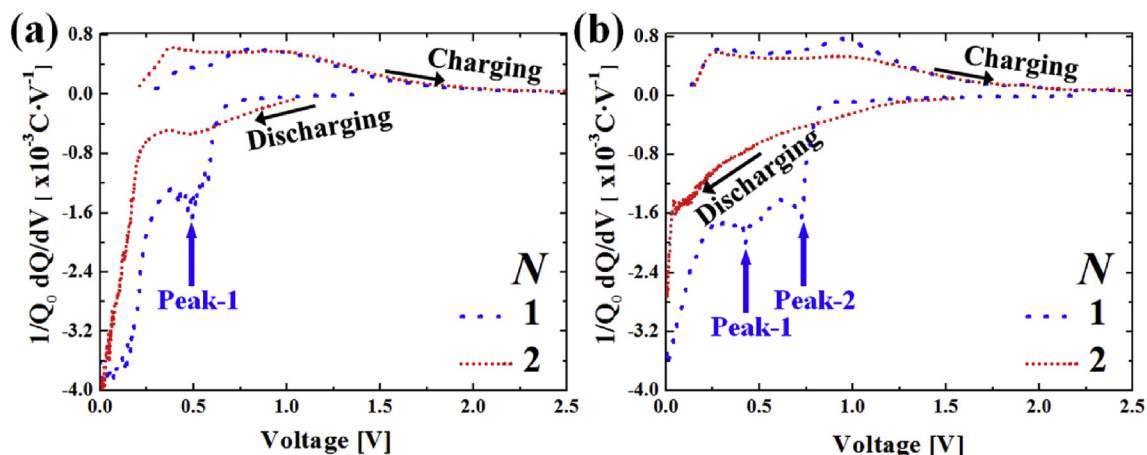


Fig. 6. Differential capacity during charge/discharge for (a) Fe-1 and (b) Fe-2 under the current rate of 500 mA g⁻¹.

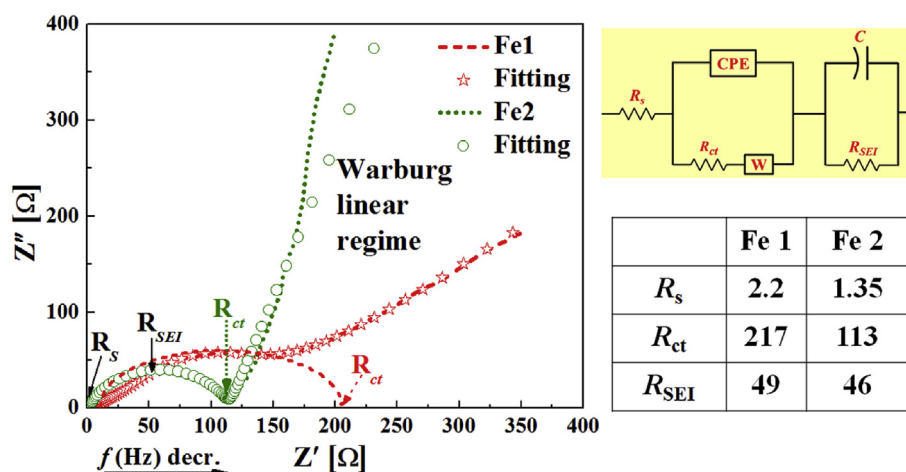


Fig. 7. The Nyquist plot for Fe-1 and Fe-2.

solution blown sample is greater. The specific capacity of rGO alone without any fibers is relatively low, as seen in Fig. S3(b). However, the results in Fig. 5(b) show that addition of rGO together with the solution blown nanofibers yields the highest specific capacity.

A stable reversible capacity of 698 mAh·g⁻¹ was obtained at $N = 80$ after the rate capability test. Reversible capacities of 588, 447, 349, and 216 mAh·g⁻¹ were observed for the Fe-2 sample at respective current densities of 500, 1000, 2000, and 5000 mA g⁻¹, as shown in Fig. 5(c). The reversible capacity of 655 mAh·g⁻¹ was retained by Fe-2 when the current rate was again lowered to 500 mA g⁻¹. Thus, sample Fe-2, which uses the rGO/Fe–Fe₃C anode, exhibited much better rate performance than achieved with the Fe–Fe₃C (Fe-1) anode and also shows a four-fold higher capacity at 5000 mA g⁻¹. The long-term cycling performance of the nanofibers at the high current density of 1500 mA g⁻¹ is shown in Fig. 5(d), along with the corresponding Coulombic efficiencies. The discharge capacity of the electrode was 558 mAh·g⁻¹ after 200 cycles at 1500 mA g⁻¹, demonstrating its excellent capacity retention at high discharge-charge rate. No discernible deterioration or damage of the electrodes was observed after 200 cycles based on SEM evaluation (Fig. S4). The long-term cycling capacity at low current density (200 mA g⁻¹) was also measured (supporting information Fig. S5), demonstrating a reversible capacity of 992 mAh·g⁻¹ after 60 cycles. Hence, it is clear that the enhanced conductivity derived from the addition of rGO and the catalytic effect of Fe₃C [11] together contribute to achieving a higher capacity at both low

and high current density. The developed rGO/Fe–Fe₃C (Fe-2) nanofibers demonstrate high specific capacity as well as remarkable rate capability and capacity retention relative to the previously reported Fe₃C-based composite electrode materials presented in Table 1.

The dQ/dV curves of Fe-1 and Fe-2 are shown in Fig. 6(a) and (b), respectively, which provides information regarding the electrochemical reactions. The curves exhibit severe undulation for $N = 1$, indicating formation of SEI layers [19]. For $N = 2$, curves are smoother in shape, suggesting that the SEI has stabilized. In Fig. 6(a), peak-1 at 0.5 V indicates the SEI formation due to Fe₃C. In Fig. 6(b), the peak-1 at 0.4 V and the peak-2 at 0.7 V indicates the SEI formation due to Fe₃C and rGO, respectively. Similar results are also reported by Su et al. with Fe@C microspheres where they highlight the peak between 0.3 and 0.8 V. Su et al. [20] concluded that Fe₃C was a better material than FeO for LIB because of lesser volume expansion of Fe₃C. In general, a reduction process causes volume expansion and contraction via separation of Fe ions from FeO. However, in Fe₃C, Fe is not readily separated from Fe₃C because of its relatively lower valence state and thus volume expansion and contraction are suppressed. From Fig. 6, no lithium insertion peaks are observed above 1 V, suggesting the absence of the Fe₂O₃ phase [21].

Electrochemical impedance spectroscopy (EIS) measurements were carried out at room temperature on both the Fe-1 and Fe-2 cells. Fig. 7 shows EIS measurements of LIB half-cells, before

cycling, over a frequency range of 100 kHz–0.1 Hz. The Nyquist data were analyzed using the Randle's equivalent circuit model, as depicted in Fig. 7. The corresponding resistance values were computed, where R_s is the solution resistance, R_{ct} is the charge transfer resistance, and R_{SEI} is the SEI layer resistance. Overall, the resistance values of Fe-2 are lower than those of Fe-1, indicating that the Fe-2 is electrically more conductive. The semi-circle shape in the Z' vs. Z'' behavior for Fe-2 indicates the lower charge transfer resistance. This low charge transfer resistance facilitates retention of high capacity even at a high current rate of 1500 mA g⁻¹. In the lower frequency range, a linear behavior is observed between Z' vs. Z'' , which is described as the Warburg impedance. A steeper slope indicates faster diffusion kinetics of Li-ions at the electrolyte-electrode interface [22].

4. Conclusions

In summary, Fe–Fe₃C nanofibers were synthesized via a cost-effective and fast supersonic blowing technique. This facile one-step method circumvents the time-consuming procedure required for nanofiber synthesis via electrospinning and allows incorporation of rGO flakes that could not readily be used in electrospinning. Compared to the rGO-free sample, the rGO/Fe–Fe₃C nanofiber exhibited improved specific capacity at high current rate. When used as an anode material for Li ion batteries, the material exhibits superior electrochemical performance in terms of its high discharge capacity, good rate capability, and excellent capacity retention, making it promising for application in lithium ion batteries.

Acknowledgement

This research was supported by the Technology Development Program to Solve Climate Changes of the National Research Foundation (NRF) funded by the Ministry of Science, ICT & Future Planning (2016M1A2A2936760), NRF-2013M3A6B1078879, and

NRF-2017R1A2B4005639.

Appendix A. Supplementary data

Supplementary data related to this article can be found at <http://dx.doi.org/10.1016/j.jallcom.2017.07.306>.

References

- [1] D. Mhamane, H.K. Kim, V. Aravindan, K.C. Roh, M. Srinivasan, K.-B. Kim, *Green Chem.* 18 (2016) 1395–1404.
- [2] Y. Sun, J. Zhang, T. Huang, Z. Liu, A. Yu, *Int. J. Electrochem. Sci.* 8 (2013) 2918–2931.
- [3] J.W. Kan, *Yong, Sci. Rep.* 3 (2013) 3502.
- [4] X. Liu, W. Si, J. Zhang, X. Sun, J. Deng, S. Baunack, S. Oswald, L. Liu, C. Yan, O.G. Schmidt, *Sci. Rep.* 4 (2014).
- [5] Y. Zhong, X. Xia, F. Shi, J. Zhan, J. Tu, H.J. Fan, *Adv. Sci.* 3 (2016) 1500286.
- [6] Y. Xiao, J.Y. Hwang, Y.K. Sun, *J. Mater. Chem. A* 4 (2016) 10379–10393.
- [7] Y.G. Huang, X.L. Lin, X.H. Zhang, Q.C. Pan, Z.X. Yan, H.Q. Wang, J.J. Chen, Q.Y. Li, *Electrochim. Acta* 178 (2015) 468–475.
- [8] X. Zhao, D. Xia, J. Yue, S. Liu, *Electrochim. Acta* 116 (2014) 292–299.
- [9] L. Su, Z. Zhou, P. Shen, *Electrochim. Acta* 87 (2013) 180–185.
- [10] Y. Tan, K. Zhu, D. Li, F. Bai, Y. Wei, P. Zhang, *Chem. Eng. J.* 258 (2014) 93–100.
- [11] J. Li, W. Wen, G. Xu, M. Zou, Z. Huang, L. Guan, *Electrochim. Acta* 153 (2015) 300–305.
- [12] S. Chen, J. Wu, R. Zhou, L. Zuo, P. Li, Y. Song, L. Wang, *Electrochim. Acta* 180 (2015) 78–85.
- [13] Y. Park, M. Oh, J.S. Park, S.-H. Baek, M. Kim, S. Kim, J.H. Kim, *Carbon* 94 (2015) 9–17.
- [14] J.G. Lee, D.Y. Kim, M.G. Mali, S.S. Al-Deyab, M.T. Swihart, S.S. Yoon, *Nanoscale* 7 (2015) 19027–19035.
- [15] H.J. Lee, W. Cho, E. Lim, M. Oh, *Chem. Commun. (Camb)* 50 (2014) 5476–5479.
- [16] X. Wang, S. Zhang, J. Li, J. Xu, X. Wang, *Inorg. Chem. Front.* 1 (2014) 641–648.
- [17] H. Huang, X. Feng, C. Du, S. Wu, W. Song, *J. Mater. Chem. A* 3 (2015) 4976–4982.
- [18] W. Xiao, Z. Wang, H. Guo, X. Li, J. Wang, S. Huang, L. Gan, *Appl. Surf. Sci.* 266 (2013) 148–154.
- [19] J. Zhu, K.Y. Ng, D. Deng, *Nanoscale* 7 (2015) 14368–14377.
- [20] L. Su, Y. Zhong, Z. Zhou, *J. Mater. Chem. A* 1 (2013) 15158.
- [21] J. Wang, H. Zhou, J. Nanda, P.V. Braun, *Chem. Mat.* 27 (2015) 2803–2811.
- [22] K. Zhang, P. Han, L. Gu, L. Zhang, Z. Liu, Q. Kong, C. Zhang, S. Dong, Z. Zhang, J. Yao, H. Xu, G. Cui, L. Chen, *ACS Appl. Mater. Interfaces* 4 (2012) 658–664.